DØ Note 6343-CONF

Updated search for Higgs boson production in dilepton plus missing transverse energy final states with 9.7 fb^{-1} of $p\overline{p}$ collisions at $\sqrt{s} = 1.96$ TeV

The DØ Collaboration
URL http://www-d0.fnal.gov
(Dated: July 1, 2012)

We present an updated search for the Standard Model Higgs boson in dilepton events with large missing transverse energy using 9.7 fb^{-1} of $p\overline{p}$ collisions at $\sqrt{s} = 1.96$ TeV, collected with the DØ detector at the Fermilab Tevatron collider. Three leptonic final states, $e^{\pm}\mu^{\mp}$, $e^{+}e^{-}$ and $\mu^{+}\mu^{-}$, are considered. No significant excess above the standard model background expectation is observed. Therefore, limits on the Higgs boson production cross section are derived at 95% CL. For M_H = 165 GeV (125 GeV), the expected limit is 0.81 (3.59) relative to the Standard Model cross section and the observed limit reaches 0.98 (4.56) in the same units.

Preliminary Results for Summer Conferences 2012

I. INTRODUCTION

In the standard model (SM), the fermions acquire mass by their interaction with the Higgs field. The Higgs field itself induces spontaneous breaking of the electroweak gauge symmetry $SU(2) \otimes U(1)$. It gives rise to massive W/Z bosons and the appearance of an additional scalar boson called the Higgs particle. This particle has yet to be discovered. Direct searches at the CERN e^+e^- collider (LEP) yield a lower limit for the SM Higgs boson mass, $M_H > 114.4$ GeV [1] at 95% confidence level (CL). A combination of results from the CDF and DØ experiments excludes the SM Higgs boson in the mass range 147 GeV $< M_H <$ 179 GeV at 95% CL [2]. Recently, the LHC experiments have explored a wide range of SM Higgs boson masses. The ATLAS collaboration excludes at 95% CL the ranges 112.9–115.5 GeV, 131–238 GeV and 251–466 GeV [3]. The CMS collaboration excludes at 95% CL the range 127-600 GeV [4]. Indirect constraints from fits to precision electroweak measurements, including the latest W boson mass measurements from CDF [5] and DØ [6], give an upper bound of $M_H < 152$ GeV [7] at 95% CL.

In this note, we present a search for the Higgs boson in final states containing two leptons ($e^{\pm}\mu^{\mp}$, e^+e^- or $\mu^+\mu^-$) and missing transverse energy ($\not\!\!E_T$), using 9.7 fb^{-1} of $p\bar{p}$ collisions collected with the DØ detector at the Fermilab Tevatron. The combination of these final states has been shown to be the most sensitive to a SM Higgs boson of mass $M_H \sim 160$ GeV [8].

The production of Higgs bosons by gluon fusion is considered, with the subsequent decay $H \to WW \to \ell\nu\ell'\nu'$, where the ℓ and ℓ' include muons and electrons, as well as τ leptons which themselves decay to muons or electrons. The contributions to the $e^{\pm}\mu^{\mp}$, e^+e^-, and $\mu^+\mu^-$ final states from weak vector boson fusion (VBF) and Higgs production in association with a vector boson (WH or ZH) are also considered, as well as gluon fusion with the decay $H \to ZZ$.

The preselection, based on the efficient reconstruction of the two leptons, is followed by additional requirements to suppress the large Drell-Yan (DY) $Z/\gamma^* \to \ell\ell$ background. In order to increase the sensitivity, the analysis is divided into jet bins. A final multivariate analysis based on a random forest of boosted decision trees (BDT) is used to separate the signal from the remaining background. The output of the BDT is the final discriminant used to search for a Higgs boson signal.

Relative to the result presented at winter 2012 conferences [9], there have been improvements to the analysis procedure in the e^+e^- and $\mu^+\mu^-$ channels: both now split the 0-jet and 1-jet multiplicity bins into a WW-depleted and a WW-enriched regions (as described later into more detail), and the e^+e^- channel includes more data, a new electron identification and an updated W+jets background estimation.

II. DØ DETECTOR

This analysis relies on the efficient identification of muons, electrons, jets and missing transverse energy using many subsystems of the DØ Run II detector [10]. The central tracking system consists of a silicon microstrip tracker [11] (SMT) and a central fiber tracker (CFT), both located within a 2 T axial magnetic field. The SMT strips have a typical pitch of 50–80 μm, and the design is optimized for tracking and vertexing over the pseudorapidity range $|\eta| < 3$, where $\eta = -\ln(\tan\theta/2)$ with θ being the polar angle relative to the proton beam direction. The system has a six-barrel longitudinal structure, with each barrel having a set of four silicon layers arranged axially around the beam pipe, interspersed with sixteen radial disks. In addition, a new layer of silicon sensors (Layer 0 [12]) was added just outside the beam pipe in 2006, and the number of radial disks was changed from sixteen to fourteen. The upgrades to the detector at this time marked the end of Run IIa and the beginning of Run IIb. The CFT has eight thin coaxial barrels, each supporting two doublets of overlapping scintillating fibers of 0.835 mm diameter, one doublet parallel to the beam axis, the other alternating by $\pm 3°$ relative to the beam axis.

A liquid-argon sampling calorimeter surrounds the central tracking system and consists of a central calorimeter (CC) covering up to $|\eta| \approx 1.1$, and two end calorimeters (EC) extending coverage to $|\eta| < 4.2$, each housed in separate cryostats. Scintillators between the CC and EC cryostats provide sampling of showers for $1.1 < |\eta| < 1.4$.

The muon system is located outside the calorimeters and consists of a layer of tracking detectors and scintillation trigger counters inside toroid magnets which provide a 1.8 T magnetic field, followed by two similar layers outside each toroid. Tracking in the muon system for $|\eta| < 1$ relies on 10 cm wide drift tubes, while 1 cm mini-drift tubes are used for $1 < |\eta| < 2$. Trigger and data acquisition systems are designed to accommodate the high luminosities of Run II. Based on preliminary information from tracking, calorimetry, and muon systems, the output of the first level of the trigger is used to limit the rate for accepted events to ≈ 1.5 kHz. The calorimeter component of the first level of the trigger has been upgraded between Run IIa and Run IIb [13]. At the next trigger stage, with more refined information, the rate is reduced further to ≈ 0.8 kHz. These first two levels of triggering rely mainly on hardware. The third and final level of the trigger, with access to all the event information, uses software algorithms and a computing farm, and reduces the output rate to ≈ 100 Hz, which is stored for further analysis.

III. DATA AND MONTE CARLO SAMPLES

The data sample used in this analysis was collected between April 2002 and September 2011 (Run II) with the DØ detector at the Fermilab Tevatron collider at $\sqrt{s} = 1.96$ TeV. It corresponds to an integrated luminosity of 9.7 fb^{-1} after imposing data quality requirements. The DØ luminosity is measured with an accuracy of 6.1% using plastic scintillator arrays located in front of the EC cryostats, covering $2.7 < |\eta| < 4.4$ [14].

Signal and SM background processes are simulated with PYTHIA [15] or ALPGEN [16] using the CTEQ6L1 [17] parton distribution functions (PDF), followed by a detailed GEANT-based [18] simulation of the DØ detector. In order to model the effects of multiple $p\overline{p}$ interactions, the Monte-Carlo (MC) samples are overlaid with events from random $p\overline{p}$ collisions with the same luminosity profiles as the data and then reconstructed with the same software as the data. The normalization of generated samples is scaled to match the number of events expected, based on the cross sections, which are calculated at the highest available order. For the gluon fusion $gg \to H$ process, the cross-section is calculated at NNLO+NNLL level [19], for WH and ZH at NNLO [20], and for vector boson fusion at NNLO in the strong coupling constant [21]. All signal cross sections are computed using the MSTW 2008 NNLO PDF set [22]. The PDF uncertainties are assessed according to recommendations of Ref. [23]. The distribution of the transverse momentum of the Higgs boson generated in the gluon fusion process is tuned to match the transverse momentum as calculated by the HQT generator, at NNLL and NNLO accuracy [24].

The main background processes for this analysis are diboson production (WW, WZ and ZZ), Z/γ^* production in leptonic final states, W+jets/γ production, $t\bar{t}$ production, and multijet production with jets misidentified as leptons. We use ALPGEN for the W+jets and Z+jets backgrounds, and PYTHIA for diboson and $t\bar{t}$ production. The background MC samples for inclusive W and Z production are normalized using NNLO cross sections calculations of Ref. [25] using the NLO CTEQ 6.1 PDF. The Z boson $p_{\rm T}$ distribution is modeled to match the distribution observed in data [26]. We also derive a residual correction for each jet multiplicity bin for this distribution. We correct the $p_{\rm T}$ distribution of the W boson based on measured $p_{\rm T}$ of the Z boson spectrum [26], taking into account the ratio between the W and Z bosons $p_{\rm T}$ distributions at NLO [27].

In the e^+e^- and $e^\pm\mu^\mp$ channels, the W+jets sample includes contributions from events where a fake electron originates from a jet or a photon. The size of each of these contributions is corrected using a data-driven method in a W+jets enriched control sample, defined with events with two leptons of the same sign and $M_T^{\rm min} > 30\,{\rm GeV}$, $\not\!\!E_T > 20\,{\rm GeV}$, $M \in [15\,{\rm GeV}, 80\,{\rm GeV}]$, and $\Delta\phi(l_1, l_2) < 3$. $M_T^{\rm min}$ is the minimum transverse mass $M_T^{\rm min} = \min(M_T^{\ell_1}, M_T^{\ell_2})$ where the transverse mass is defined as $M_T = \sqrt{2 \cdot p_{\rm T}^\ell \cdot \not\!\!E_T \cdot (1 - \cos\Delta\phi(\ell, \not\!\!E_T))}$, M is the invariant mass of the two electrons, $\not\!\!E_T$ is the missing transverse energy and $\Delta\phi(l_1, l_2)$ is the azimuthal opening angle between the two leptons.

In the $e^\pm\mu^\mp$ channel, the correction is derived comparing the number of hits in the innermost silicon layer (Layer 0) between the Run IIb data and MC, and applied to both Run IIa and Run IIb MC samples. In the e^+e^- channel, a similar method was used, except that several variables (such as $\not\!\!E_T$ or the invariant mass of the two electrons) were combined into two decision trees to derive the correction. One of these discriminants was trained to discriminate W+jets from W+photon events, and the other one was trained to discriminate, among the latter population, if the photon originates from initial or final state radiation.

Approximate NNLO calculations [28] are used for $t\bar{t}$ production cross-section, while the NLO WW, WZ and ZZ production cross section values are taken from Ref. [29]. For the main source of background, WW production, the $p_{\rm T}$ of the diboson system is modeled using the MC@NLO simulation [30] and the distribution of the opening angle of the two leptons is corrected to take into account the contribution from gluon fusion [31].

The background due to multijet production, where jets are misidentified as leptons, is determined from data. In order to obtain a high-statistics sample of predominantly multijet events, the lepton quality requiremens in each channel are inverted. The multijet sample has to be scaled to the actual contribution in the signal region in order to account for any kinematic bias introduced from reversing the lepton quality requirements (muon quality, electron likelihood or BDT discriminant, see Section IV). To derive the scale factor, the multijet sample is compared to events which pass all the signal requirements except that a like-charge requirement is imposed. As the probability of a jet faking a lepton (fake rate) is independent of charge, assuming a small charge correlation between the leptons in multijet events, the like-charge sample has the same normalization and kinematics as the actual multijet contribution. The fake rate depends on the jet multiplicity and therefore the multijet background is estimated separately for each jet multiplicity. A systematic uncertainty is assigned to the multijet prediction to account for the assumption of the lack of charge correlation between the leptons and the contribution of non-multijet processes in the reversed lepton quality sample.

IV. PRESELECTION

All events satisfying any trigger of the DØ trigger suite are accepted in this analysis. While most events selected in the analysis are selected by single-lepton and dilepton triggers, additional acceptance is gained by including triggers with jets or missing transverse energy. The simulated background samples are normalized to the number of expected events, based on the integrated luminosity and cross section. Various inefficiencies, for instance due to trigger and lepton identification, are corrected using a Drell-Yan dominated sample, by comparing the number of MC and data events. This procedure is repeated also for each jet multiplicity, to derive a jet bin dependent Drell-Yan background normalization, because the dependence on jet multiplicity of the cross-section of this background is not well known.

Electrons are identified using calorimeter and tracking information. Electromagnetic showers are identified in the calorimeter by comparing the longitudinal and transverse shower profiles to those of simulated electrons. The showers must be isolated, deposit more than 90% of their energy in the electromagnetic part of the calorimeter and pass a boosted decision tree (BDT, e^+e^- channel) or likelihood ($e^\pm\mu^\mp$ channel) criterion that includes a spatial track match and, in the central detector region, an E/p requirement, where E is the energy of the calorimeter cluster and p is the momentum of the track. The value of the BDT discriminant (EMV) or likelihood variable is referred to as the electron quality. Electrons are required to be in the acceptance of the calorimeter ($|\eta| < 1.1$ or $1.5 < |\eta| < 2.5$). In the dielectron channel, events with one electron in the end-cap calorimeter (EC) are treated separately from events with both electrons in the central calorimeter (CC). This improves the analysis sensitivity as the background composition is different in the two pseudorapidity regions. Events where both electrons are in the EC are not considered in the analysis due to large background and a small signal contribution. The transverse momentum of electrons is obtained from energy deposits in the calorimeter.

Muon tracks are reconstructed from hits in the wire chambers and scintillators in the muon system and must match a track in the central tracker. The numbers of hits in the wire chambers and in the scintillators are combined to define a muon quality variable, used in the final stage of the analysis. Muons are restricted to the fiducial coverage of the muon system $|\eta| < 2.0$. To select isolated muons, the scalar sum iso_{track} of the transverse momentum of all tracks, other than that of the muon, is calculated in a cone of $\mathcal{R} = 0.5$ around the muon track. Here, $\mathcal{R} = \sqrt{(\Delta\phi)^2 + (\Delta\eta)^2}$. The transverse energy deposited in the calorimeter in a hollow cone of $0.1 < \mathcal{R} < 0.4$ around the muon is also measured and denoted iso_{cal}. In the $e^\pm\mu^\mp$ final state, both quantities are required to be smaller than $0.15 \times p_{\rm T}^\mu$, where $p_{\rm T}^\mu$ is the transverse momentum of the muon. In the dimuon final state, the track isolation (iso_{track}) is required to be less than $0.25 \times p_{\rm T}^\mu$ and the calorimeter isolation (iso_{cal}) is required to be less than $0.4 \times p_{\rm T}^\mu$. In addition, the calorimeter isolation for each muon is required to be $iso_{cal} < 10$ GeV. If the other lepton is closer than $\Delta\mathcal{R} = 0.5$, the isolation variables are recomputed by removing the contribution of the other lepton. This prevents the presence of one lepton to spoil the isolation of the other one. Muons from cosmic rays are rejected by requiring a timing criterion on the hits in the scintillator layers as well as by applying restrictions on the position of the muon track with respect to the selected $p\bar{p}$ interaction point (primary vertex).

Hadronic jets are reconstructed from energy deposits in the calorimeter towers using an iterative midpoint cone algorithm with a cone radius of 0.5 [32]. All calorimeter jets are required to pass a set of quality criteria which are approximately 98% efficient and at least two reconstructed tracks are required to be within ΔR(track, jet-axis)$\leq$0.5. Jets are also required to originate from the $p\bar{p}$ primary vertex (for RunIIb only).

Missing transverse energy, $\not\!\!E_T$, is obtained from a vector sum of transverse components of calorimeter energy depositions and is corrected for identified muons. Jet energies are calibrated using transverse momentum balance in photon+jet events [33], and the correction is propagated to $\not\!\!E_T$.

We select events where the two leptons with highest $p_{\rm T}$ (ℓ_1 and ℓ_2) have opposite charge and originate from the same position (within 2 cm) along the beamline; any additional reconstructed lepton is not considered for the $\mu^+\mu^-$ channel, whereas in the $e^\pm\mu^\mp$ and e^+e^- channels, events with two electrons and one muon or one electron and two muons are vetoed. The requirements for the transverse momenta of the two leptons are the following: in the e^+e^- and $\mu^+\mu^-$ channels we select $p_{\rm T}^{\ell 1} > 15$ GeV and $p_{\rm T}^{\ell 2} > 10$ GeV, while in the $e^\pm\mu^\mp$ channel we select $p_T^\mu > 10$ GeV and $p_{\rm T}^e > 15$ GeV. In addition, the dilepton invariant mass is required to exceed 15 GeV in the e^+e^- and $\mu^+\mu^-$ channels. This stage of the analysis is referred to as "preselection". Figures 1-3 show several kinematic distributions from each dilepton channel after preselection.

Signal and background composition changes with the jet multiplicity. The sensitivity of the analysis is greatly improved by splitting the events according to the jet multiplicity: no jet, one jet, or two or more jets. The number of events in each jet multiplicity bin at this stage can be found in Table I. In general, good agreement between data and the total expected background contribution is observed. The Z/γ^* contribution and multijet events are the dominant background sources after preselection.

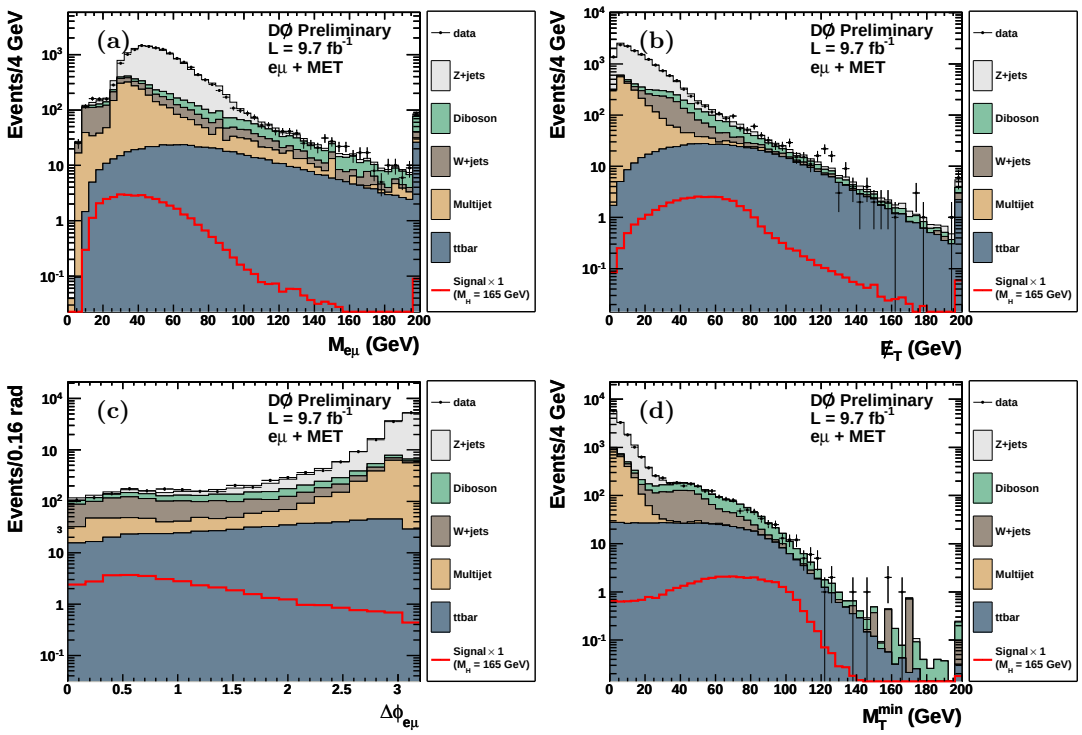

FIG. 1: The (a) dilepton mass, (b) $\not\!\!E_T$, (c) $\Delta\phi$ between the leptons, and (d) minimum transverse mass between either lepton and the $\not\!\!E_T$, for the $e^{\pm}\mu^{\mp}$ channel after preselection. The last bin includes all events above the upper range of the histograms (a), (b), (d).

TABLE I: Expected and observed number of events for each jet multiplicity bin after preselection in the $e^{\pm}\mu^{\mp}$, e^+e^- and $\mu^+\mu^-$ final states. The signal assumes a Higgs boson mass of 165 GeV for each jet bin.

	Data	Total background	Signal	$Z \to ee$	$Z \to \mu\mu$	$Z \to \tau\tau$	$t\bar{t}$	W+jets	Diboson	Multijet
$e^{\pm}\mu^{\mp}$:										
0 jet	12131	12265.7	21.5	343.7	1036.0	7468.3	17.8	960.8	728.4	1710.7
1 jet	2039	2123.7	10.9	54.0	147.5	998.6	174.8	173.7	152.6	422.4
≥ 2 jets	766	751.2	5.3	7.2	24.0	148.7	408.7	57.1	25.3	80.2
e^+e^-:										
0 jet	572831	575627.0	11.4	567098.4	-	4717.4	17.6	613.1	520.6	2659.9
1 jet	75461	75904.3	6.6	73832.2	-	710.1	99.9	152.1	259.0	850.9
≥ 2 jets	11449	11604.7	4.5	10959.3	-	117.6	139.2	37.0	173.0	178.6
$\mu^+\mu^-$:										
0 jet	701086	703354.3	14.1	-	694950.3	5612.6	11.3	359.2	666.2	1754.7
1 jet	95906	96440.8	8.1	-	94828.8	691.6	102.5	76.5	321.7	419.7
≥ 2 jets	16483	16955.4	6.5	-	16177.2	108.0	280.6	14.6	270.1	104.9

V. FINAL SELECTION

The e^+e^- and $\mu^+\mu^-$ channels use a random forest BDT discriminant to remove the dominant Z/γ^* background at the preselection level (DY BDT). The BDT is trained for each Higgs mass point considered in each jet multiplicity bin separately for e^+e^- and $\mu^+\mu^-$ channels. The output of the BDT is a single number, which characterizes the event as background-like or signal-like. We use 200 randomized trees with no pruning, and we use the bagging algorithm for boosting (see Ref. [34]).

The following list of input variables are used for the 0-jet DY BDT:

- $p_{\rm T}$ of ℓ_1;

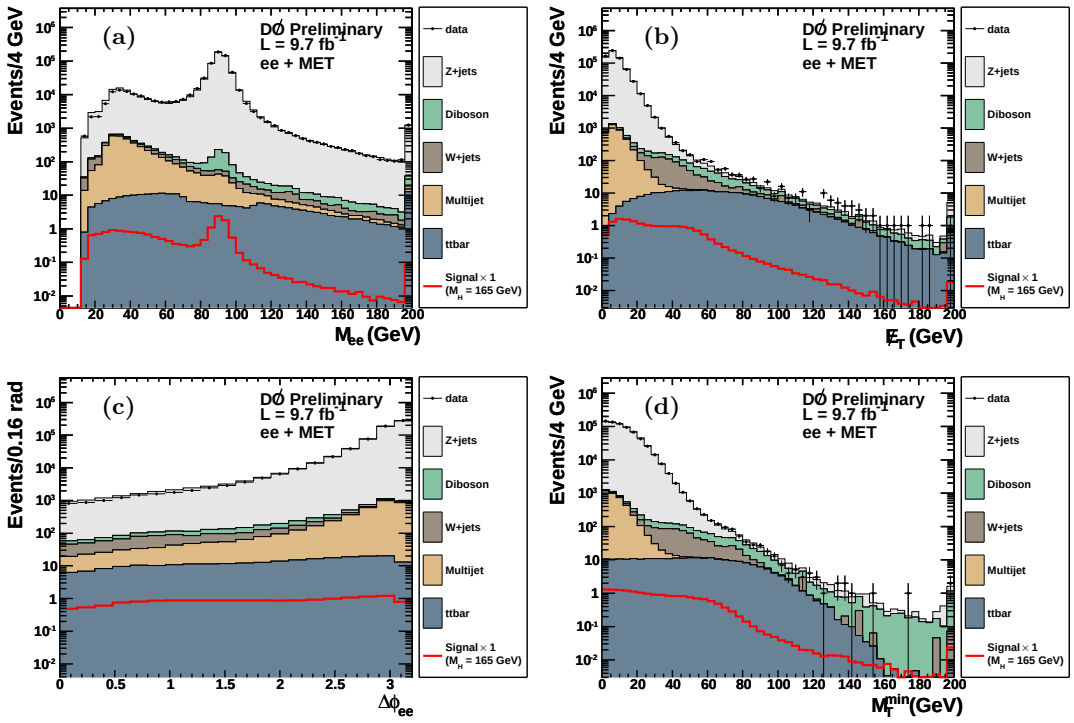

FIG. 2: The (a) dilepton mass, (b) $\not\!\!E_T$, (c) $\Delta\phi$ between the leptons and (d) minimum transverse mass between either lepton and the $\not\!\!E_T$ for the e^+e^- channel after preselection. The last bin includes all events above the upper range of the histograms (a), (b), (d).

- p_{T} of ℓ_2;
- the product of charge and pseudorapidity for ℓ_1;
- the product of charge and pseudorapidity for ℓ_2;
- invariant mass of the two leptons;
- azimuthal opening angle between the two leptons, $\Delta\phi(\ell_1, \ell_2)$;
- opening angle in η and ϕ space between the two leptons, $\Delta R(\ell_1, \ell_2)$;
- $\not\!\!E_T$;
- $\not\!\!E_T^{\,\mathrm{special}} = \begin{cases} \not\!\!E_T & \text{if } \Delta\phi(\not\!\!E_T,\ \text{nearest lepton or jet}) > \pi/2 \\ \not\!\!E_T \times \sin(\Delta\phi(\not\!\!E_T,\ \text{nearest lepton or jet})) & \text{otherwise} \end{cases}$
- minimum transverse mass M_T^{min}between $\not\!\!E_T$ and each lepton;
- minimum of azimuthal angle difference between $\not\!\!E_T$ and each lepton;
- maximum of azimuthal angle difference between $\not\!\!E_T$ and each lepton;
- transverse mass between $\not\!\!E_T$ and dilepton pair, $M_T(\ell_1\ell_2, \not\!\!E_T)$;
- M_{T2}, an extension of the transverse mass to a final state with two visible and two invisible particles [35];

The 1-jet DY-BDT uses in addition the following variables:

- $\not\!\!E_T^{\,\mathrm{Scaled}} = \not\!\!E_T / \sqrt{\sum_{\mathrm{jets}} \left(\Delta E^{\mathrm{jet}} \cdot \sin\theta^{\mathrm{jet}} \cdot \cos\Delta\phi\left(\mathrm{jet}, \not\!\!E_T\right)\right)^2}$ (where ΔE is the jet energy resolution);
- jet p_{T};

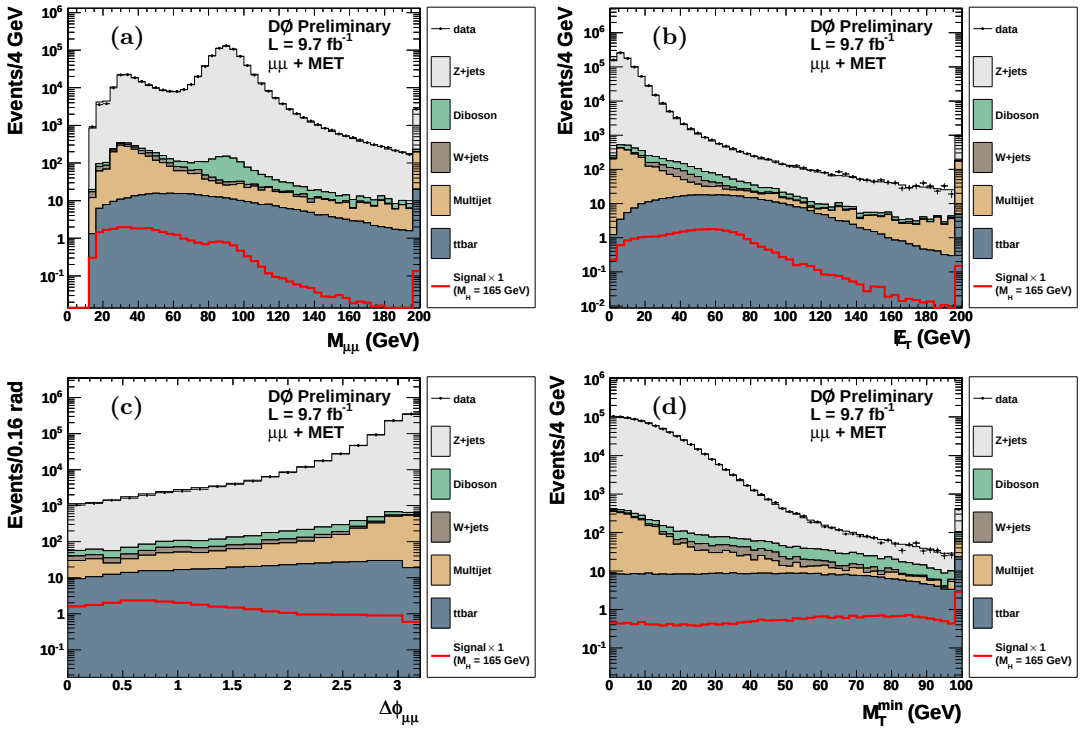

FIG. 3: The (a) dilepton mass, (b) $\not\!\!E_T$, (c) $\Delta\phi$ between the leptons and (d) minimum transverse mass between either lepton and the $\not\!\!E_T$ for the $\mu^+\mu^-$ channel after preselection. The last bin includes all events above the upper range of the histograms (a), (b), (d).

- azimuthal angle difference between $\not\!\!E_T$ and the jet;

The 2-jet DY-BDT uses all of the variables for the 0-jet DY-BDT, the jet quantities used in the 1-jet DY-BDT for the two highest p_T jets (j_1 and j_2), and the following additional variables:

- absolute value of the rapidity difference between the jets, $\Delta\eta(j_1, j_2)$;
- invariant mass of the two jets, $M(j_1, j_2)$;

The DY-BDT discriminant for $m_H = 125$ GeV is shown in Fig. 4 and for $m_H = 165$ GeV in Fig. 5. To reject most of the Z/γ^* background, we require that the discriminant output is greater than a particular value. This value varies for each Higgs mass point in each jet bin and is chosen to have a constant Z/γ^* background rejection for all mass points.

The $e^\pm\mu^\mp$ channel does not utilize a BDT discriminant to remove the Z/γ^* background, but instead applies kinematic requirements to reduce the dominant backgrounds after preselection. For the signal, large missing transverse energy is expected due to neutrinos in the final state. This is not the case for multijet and $Z/\gamma^* \to \tau\tau$ events. In addition, the missing transverse energy is not expected to be aligned with any of the leptons for the signal while this is the case for Z/γ^* as well as multijet events. For the latter, the missing transverse energy is mostly caused by the mismeasured energy of fake leptons, thus the missing transverse energy tends to point in the direction of the fake leptons. In $Z/\gamma^* \to \tau\tau$ events, charged leptons and neutrinos follow the direction of the tau leptons due to the large boost, thus the missing transverse energy is also expected to be aligned with the leptons. A quantity that takes into account both the absolute value of the missing transverse energy as well as the angle to the leptons is the minimum transverse mass, $M_T^{\rm min} = \min(M_T^e, M_T^\mu)$, and is expected to peak at lower values for Z/γ^* and multijet events compared to the signal. Thus, for the $e^\pm\mu^\mp$ events a minimum transverse mass exceeding 20 GeV is required, which rejects the majority of the Z/γ^* and multijet backgrounds. An additional requirement of $M_{\rm T2} > 15$ GeV further reduces these backgrounds. The distributions of $M_T^{\rm min}$and $M_{\rm T2}$ for the $e^\pm\mu^\mp$ final state after preselection are shown in Fig. 6 for each jet multiplicity bin.

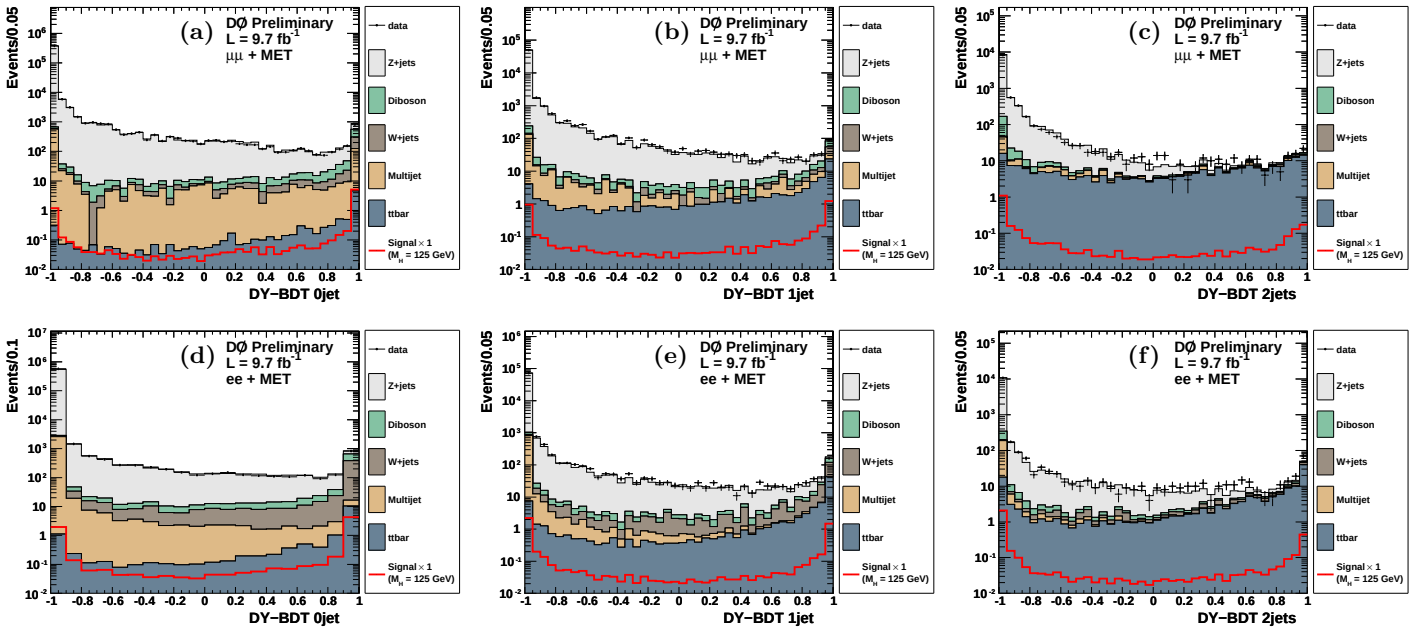

FIG. 4: DY BDT discriminant for $\mu^+\mu^-$ channel in the (a) 0-jet bin, (b) 1-jet bin, (c) $\geq$ 2-jet bin and corresponding distributions for the e^+e^- channel in the (d) 0-jet bin, (e) 1-jet bin and (f)$\geq$ 2-jet bin. The discriminant shown is trained for a Higgs mass of 125 GeV. For the final selection a requirement at 0.45, 0.25 and -0.25 (0.95, -0.5 and -0.85) is applied in these distributions for the 0-jet, 1-jet and $\geq$ 2-jet bin and in the e^+e^- ($\mu^+\mu^-$) analysis respectively.

TABLE II: Expected and observed number of events for each jet multiplicity bin after the final selection in the $e^\pm\mu^\mp$, e^+e^-, and $\mu^+\mu^-$ final states, assuming $m_H = 165$ GeV for each jet bin. The numbers in brackets correspond to the efficiency of the final selection with respect to the preselection, shown in Table I, for both the total background and signal. The uncertainty quoted on the total background combines both statistical and systematic uncertainties.

	Data	Total background		Signal		$Z \to ee$	$Z \to \mu\mu$	$Z \to \tau\tau$	$t\bar{t}$	W+jets	Diboson	Multijet
$e^\pm\mu^\mp$:												
0 jet	1266	1334.1 ± 128	(10.9%)	20.1	(93.5%)	6.3	54.6	7.5	12.5	714.7	522.6	15.8
1 jet	367	339.8 ± 44	(16.0%)	9.3	(85.3%)	3.2	13.4	2.9	108.8	106.0	93.83	11.7
≥ 2	321	307.1 ± 43	(40.9%)	4.1	(77.4%)	0.96	2.8	0.91	250.9	35.0	12.24	4.2
e^+e^-:												
0 jet	1232	1279.9 ± 141	(0.2%)	10.3	(90.4%)	505.4	-	26.6	12.7	414.1	310.3	10.8
1 jet	388	397.6 ± 44	(0.5%)	5.0	(75.8%)	125.9	-	13.9	68.4	124.6	62.1	2.8
≥ 2 jets	232	188.4 ± 21	(1.6%)	2.4	(53.3%)	40.7	-	7.1	110.3	18.5	11.2	0.7
$\mu^+\mu^-$:												
0 jet	749	817.1 ± 104	(0.1%)	11.7	(83.0%)	-	257.8	3.7	4.6	175.4	261.1	114.5
1 jet	660	634.1 ± 99	(0.7%)	5.9	(72.8%)	-	389.1	30.1	62.9	39.0	75.7	37.3
≥ 2 jets	809	816.7 ± 146	(4.8%)	3.6	(55.4%)	-	562.2	11.1	189.8	8.9	27.5	16.6

The number of events at the final selection stage for each of the dilepton states are shown in Table II. In general, good agreement between data and the remaining backgrounds is observed. Figs. 7-9 show several kinematic distributions from each dilepton channel after final selection.

In order to constrain the irreducible WW background, the zero and one jet multiplicity bins are split into a WW-depleted and a WW-enriched region in the e^+e^- and $\mu^+\mu^-$ analyses. This splitting is performed using a boosted decision tree trained with the same settings and input variables as the final discriminant described in Section VI, except that it is trained to recognize diboson WW events instead of Higgs events. The output of this discriminant is shown in Fig. 10 and 11 at final selection. The splitting discriminant value is defined by finding the maximum significance of the WW background in the 0 and 1 jet multiplicity bins for the WW-enriched region. The cut value applied to separate the WW-depleted from the WW-enriched region is 0.92 (0.68) and 0.7 (0.6) for the 0 jet (1 jet)

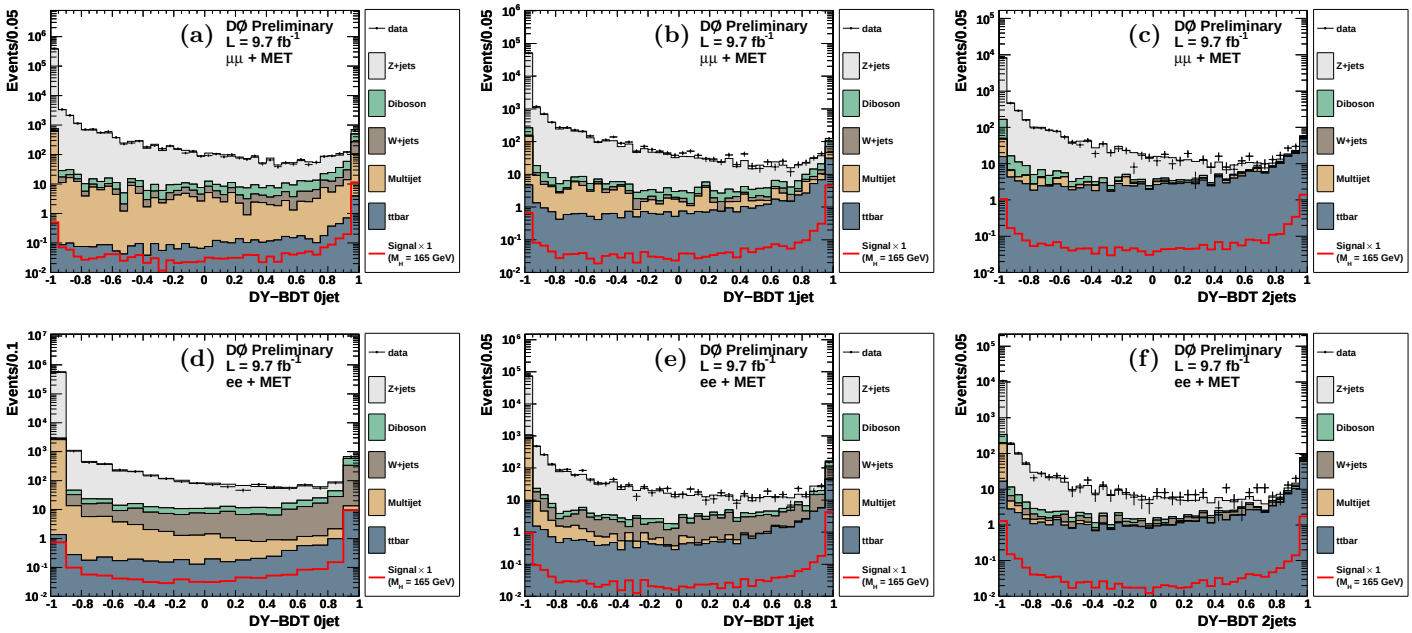

FIG. 5: DY BDT discriminant for $\mu^+\mu^-$ channel in the (a) 0-jet bin, (b) 1-jet bin, (c) $\geq$ 2-jet bin and corresponding distributions for the e^+e^- channel in the (d) 0-jet bin, (e) 1-jet bin and (f)$\geq$ 2-jet bin. The discriminant shown is trained for a Higgs mass of 165 GeV. For the final selection a requirement at 0, 0.15 and 0.05 (0.9, -0.55 and -0.7) is applied in these distributions for the 0-jet, 1-jet and $\geq$ 2-jet bin and in the e^+e^- ($\mu^+\mu^-$) analysis respectively.

multiplicity bins respectively for $\mu^+\mu^-$and e^+e^-channel. In the following we use both regions above and below the separation cut value and analyze them as separate channels. This results into a total of thirteen separate channels: three for $e^\pm\mu^\mp$ and five each (two each for 0 jet and 1 jet and one for 2 or more jets) for e^+e^- and $\mu^+\mu^-$.

VI. FINAL DISCRIMINANTS

The signal is separated from the remaining background using a final BDT. It uses all variables as input that are used for the DY discriminant as listed above with the addition of the following variables:

- e^+e^-
  - minimum EMV of the two electrons
  - number of Layer 0 hits for the minimum quality electron (Run IIb only)
  - number of Layer 0 hits for the maximum quality electron (Run IIb only)
- $e^\pm\mu^\mp$
  - likelihood used for electron identification
  - number of Layer 0 hits for the electron (Run IIb only)
  - muon quality (depends on the number of hits in the muon system, see Section IV; this variable is an integer index that increases with increasing muon identification quality)
- $\mu^+\mu^-$
  - minimum quality of the two muons
  - the track isolation of each muon

The following additional information is provided for events with jets (N_{jets}):

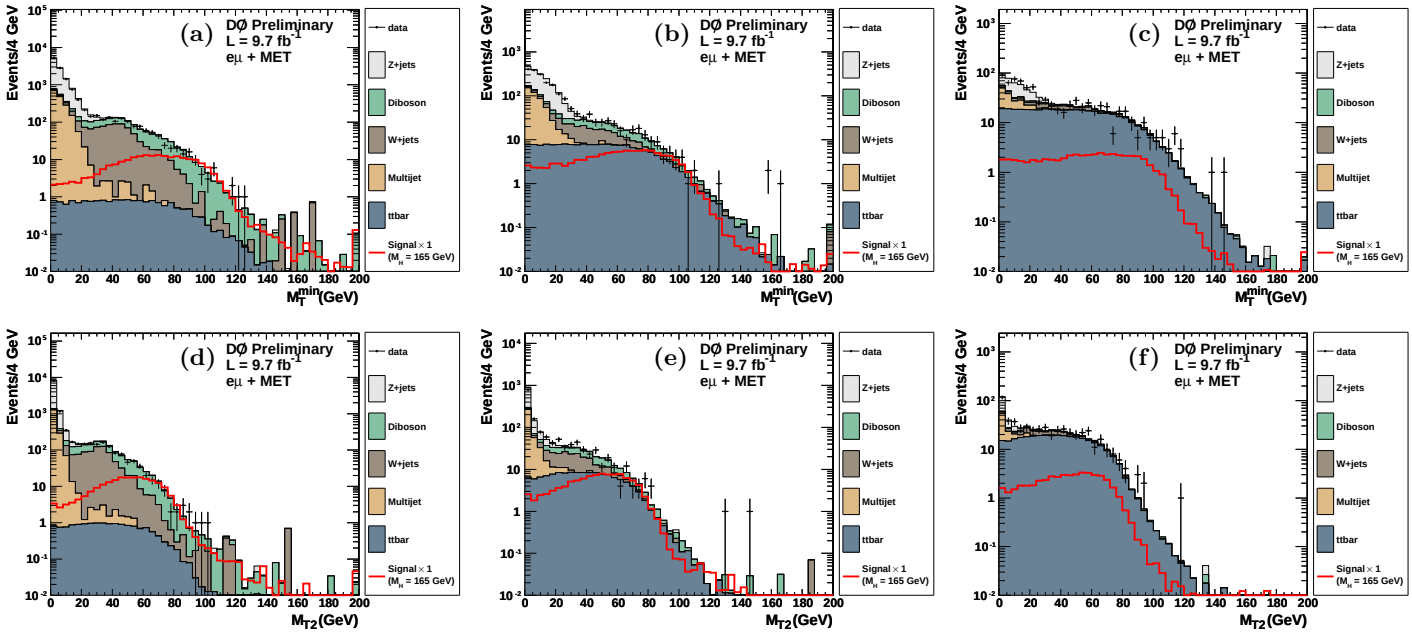

FIG. 6: $M_T^{\rm min}$distribution for the $e^{\pm}\mu^{\mp}$ channel in the (a) 0-jet bin, (b) 1-jet bin, (c) $\geq$ 2-jet bin. $M_{\rm T2}$ distribution for the $e^{\pm}\mu^{\mp}$ channel in the (d) 0-jet bin, (e) 1-jet bin, (f)$\geq$ 2-jet bin.

- Channels with $N_{\rm jets} = 1$
  - $O(b-{\rm tag})$: the output of a multivariate analysis trained to discriminate jets originating from b-quarks from those originating from light quarks [36].
- Channels with $N_{\rm jets} > 1$
  - maximum $O(b-{\rm tag})$
  - minimum $O(b-{\rm tag})$

Simulated events are used to train the BDT to differentiate between all Higgs boson signal events (including gluon gluon fusion, associated production and vector boson fusion) and all background events (diboson, $t\bar{t}$, W boson, Z/γ^*, etc.) in the three jet multiplicities (0, 1, and $\geq$2 jet bins), and for each Higgs boson mass considered. The distributions of the final discriminant for separate channels assuming $M_H = 125$ GeV is shown in Fig. 12, 14 and 16 and for $M_H = 165$ GeV in Fig. 13, 15 and 17.

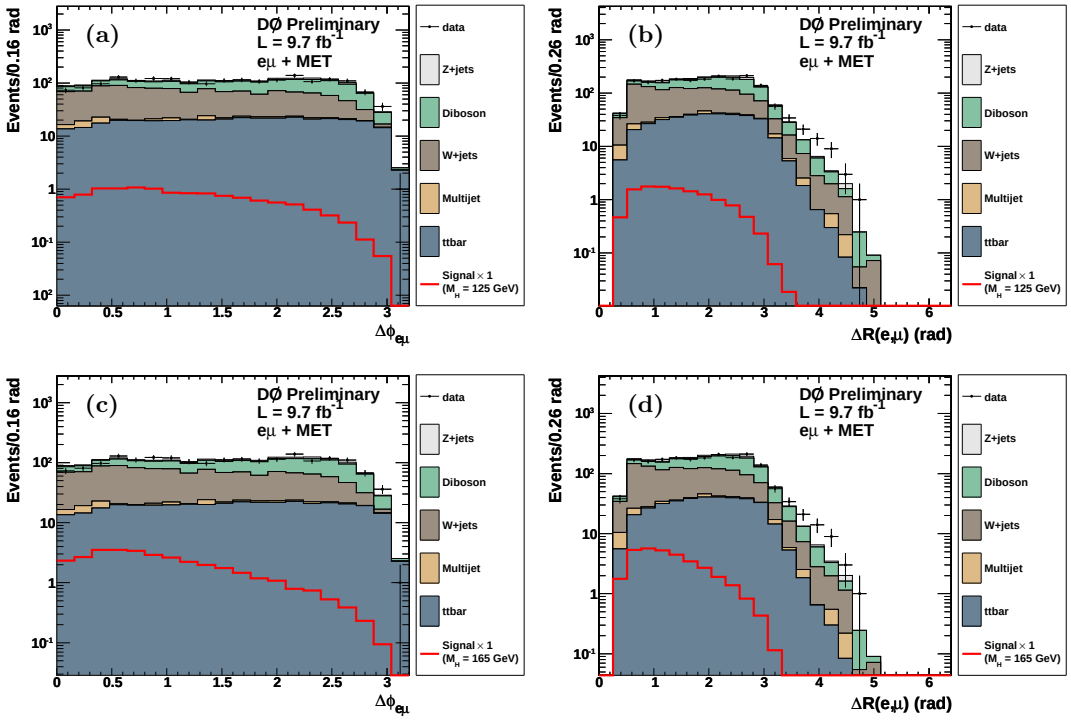

FIG. 7: The (a),(c) $\Delta\phi$ between the leptons and (b),(d) three dimensional opening angle ΔR between the leptons for the $e^{\pm}\mu^{\mp}$ channel after final selection, respectively for $m_H = 125$ GeV and $m_H = 165$ GeV.

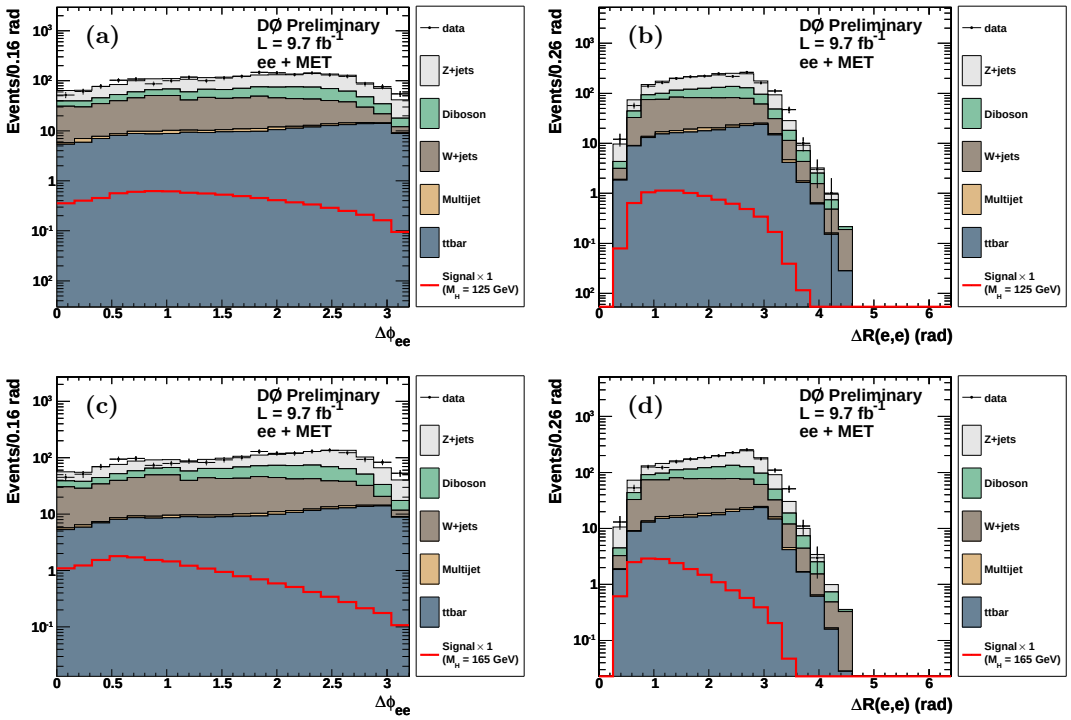

FIG. 8: The (a),(c) $\Delta\phi$ between the leptons and (b),(d) three dimensional opening angle ΔR between the leptons for the $e^{+}e^{-}$ channel after final selection, respectively for $m_H = 125$ GeV and $m_H = 165$ GeV.

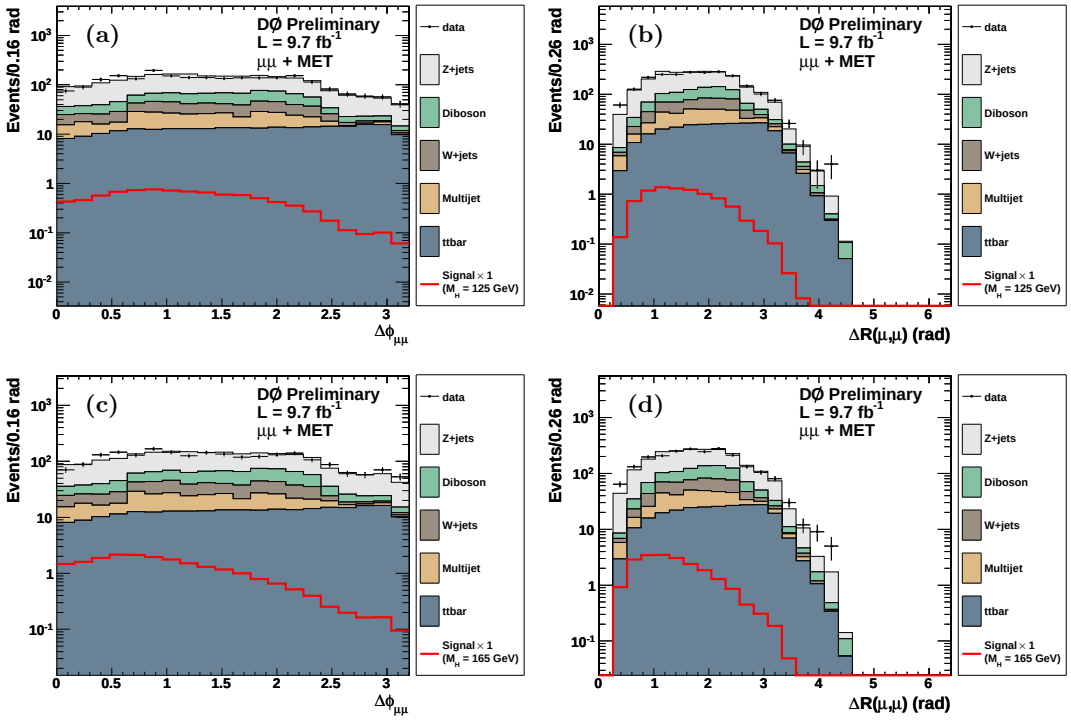

FIG. 9: The (a),(c) $\Delta\phi$ between the leptons and (b),(d) three dimensional opening angle ΔR between the leptons for the $\mu^+\mu^-$ channel after final selection, respectively for $m_H = 125$ GeV and $m_H = 165$ GeV.

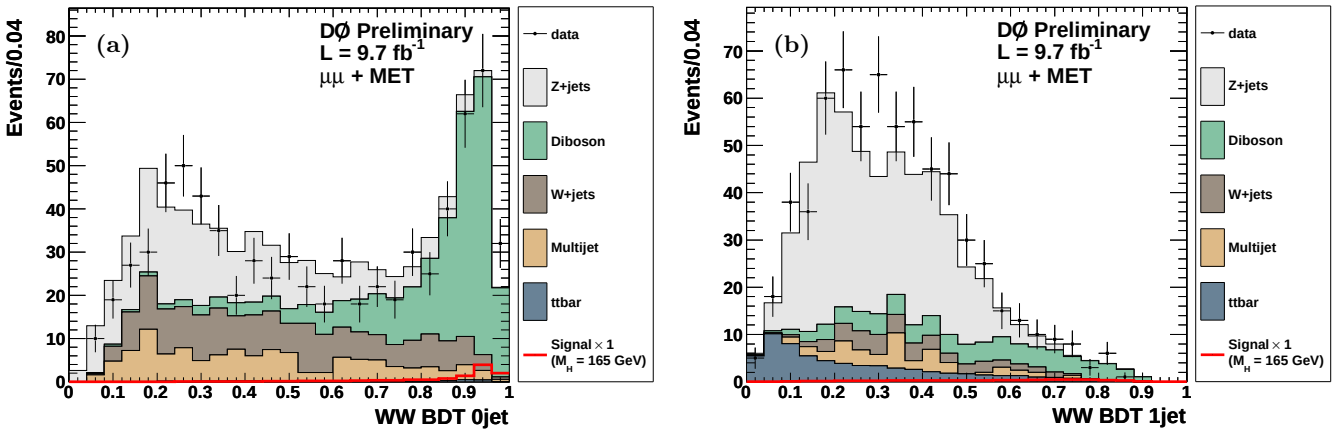

FIG. 10: The WW discriminant for the $\mu^+\mu^-$ channel with no jet (a) or one jet (b).

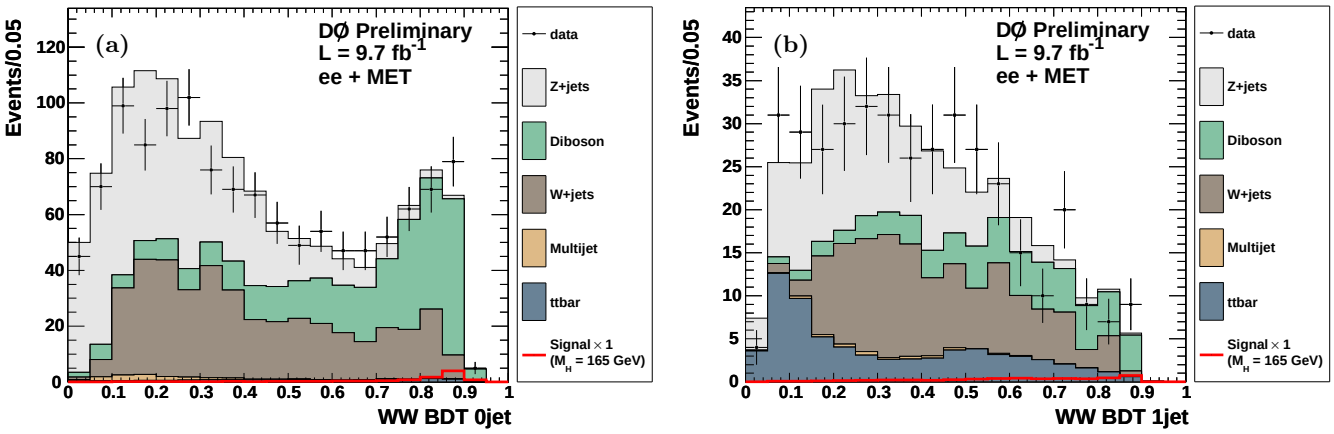

FIG. 11: The WW discriminant for the e^+e^- channel with no jet (a) or one jet (b).

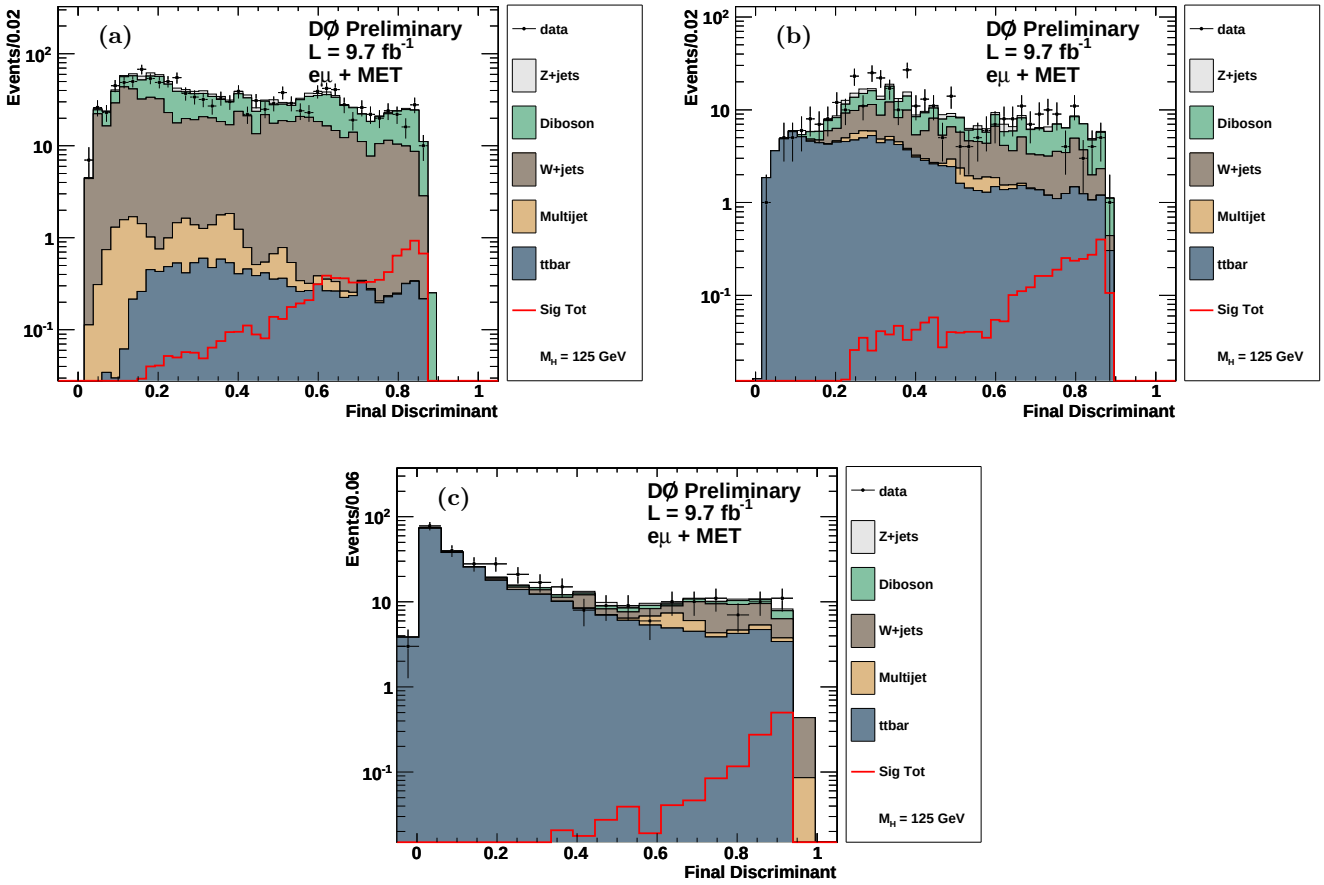

FIG. 12: The final BDT discriminant for $M_H = 125$ GeV for the $e^{\pm}\mu^{\mp}$ channel with (a) no jet, (b) one jet and (c) equal or more than 2 jets.

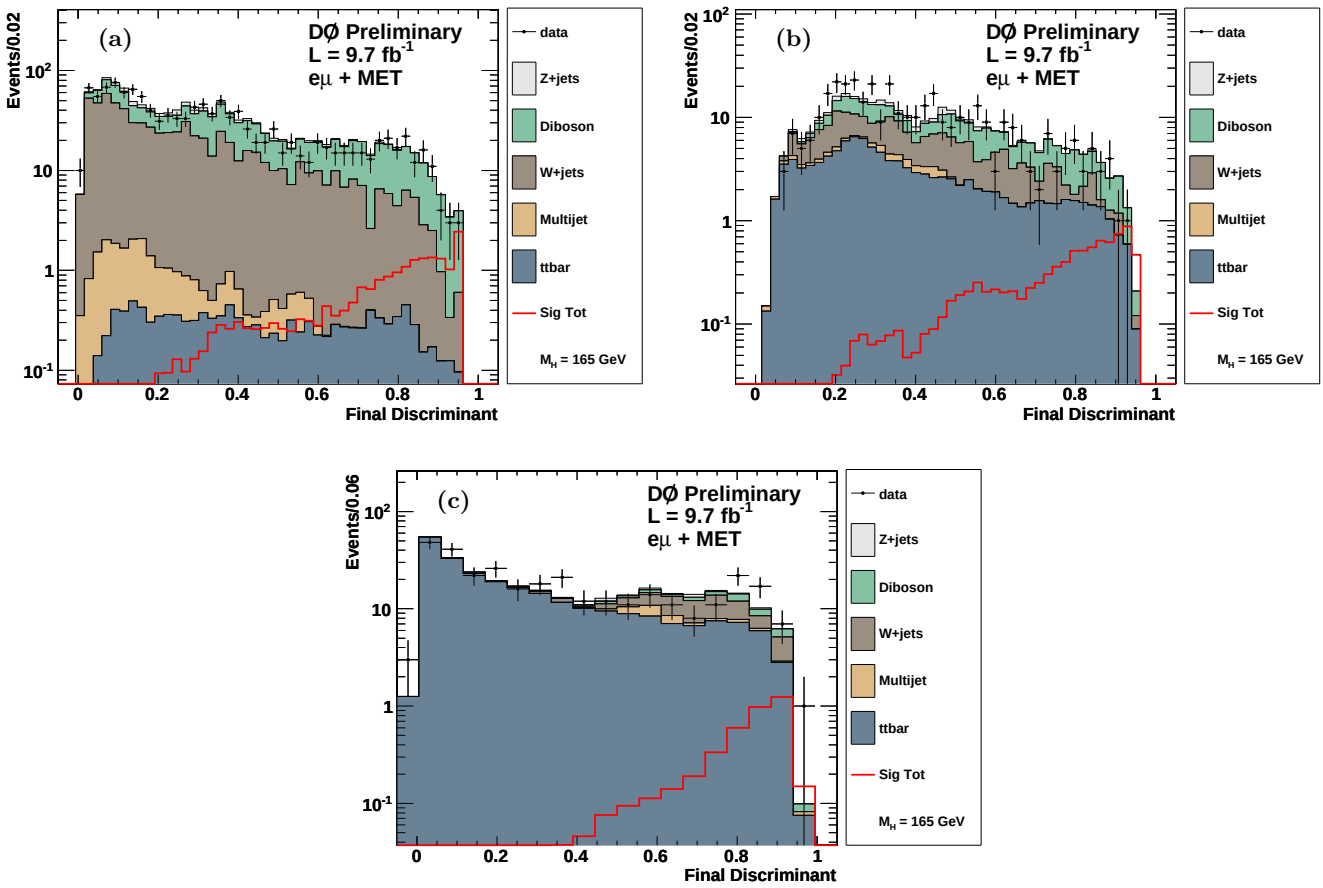

FIG. 13: The final BDT discriminant for $M_H = 165$ GeV for the $e^{\pm}\mu^{\mp}$ channel with (a) no jet, (b) one jet and (c) equal or more than 2 jets.

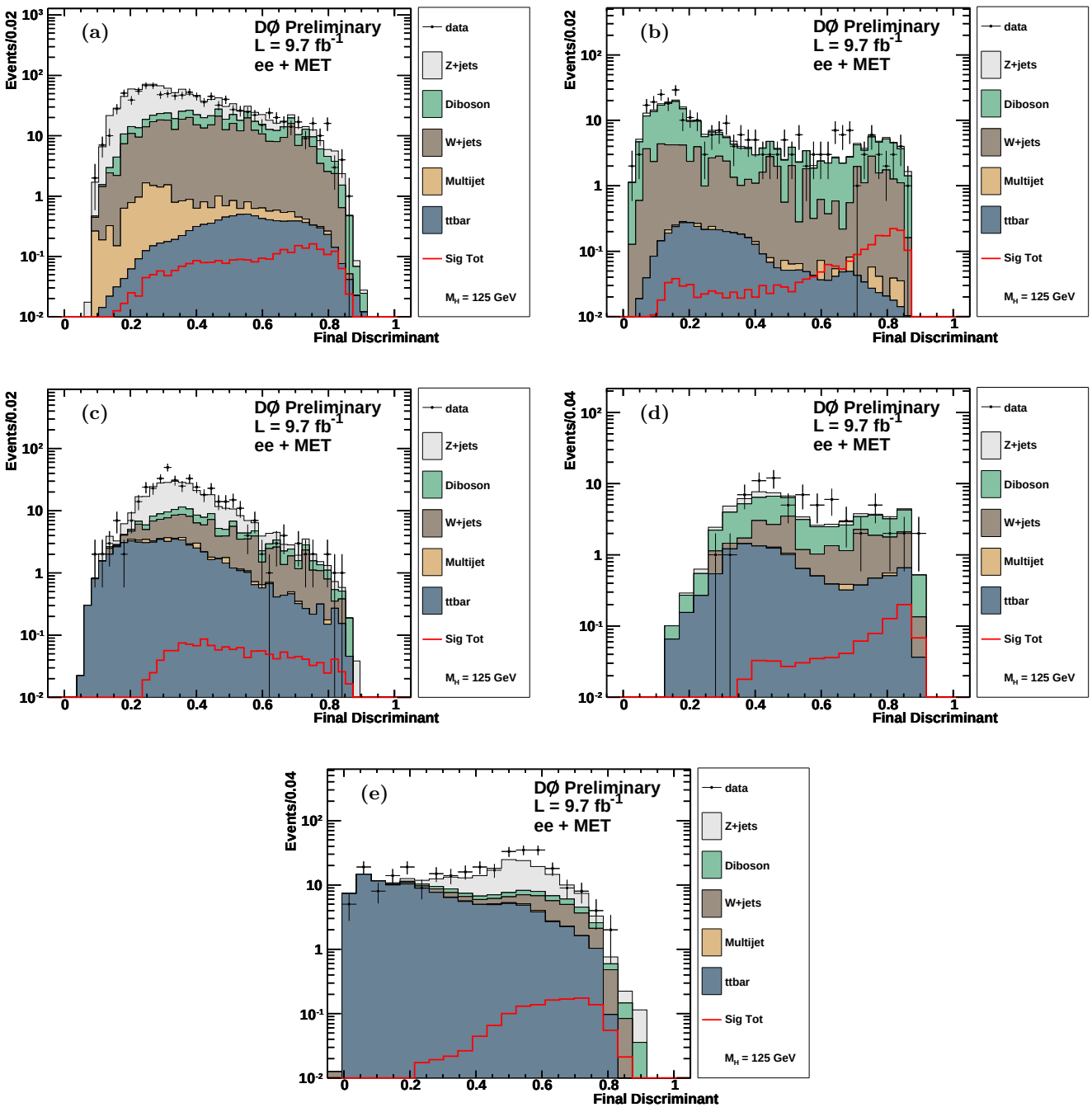

FIG. 14: The final BDT discriminant for $M_H = 125$ GeV for the e^+e^- channel with (a) no jet WW-depleted, (b) no jet WW-enriched, (c) one jet WW-depleted, (d) one jet WW-enriched and (e) equal or more than 2 jets.

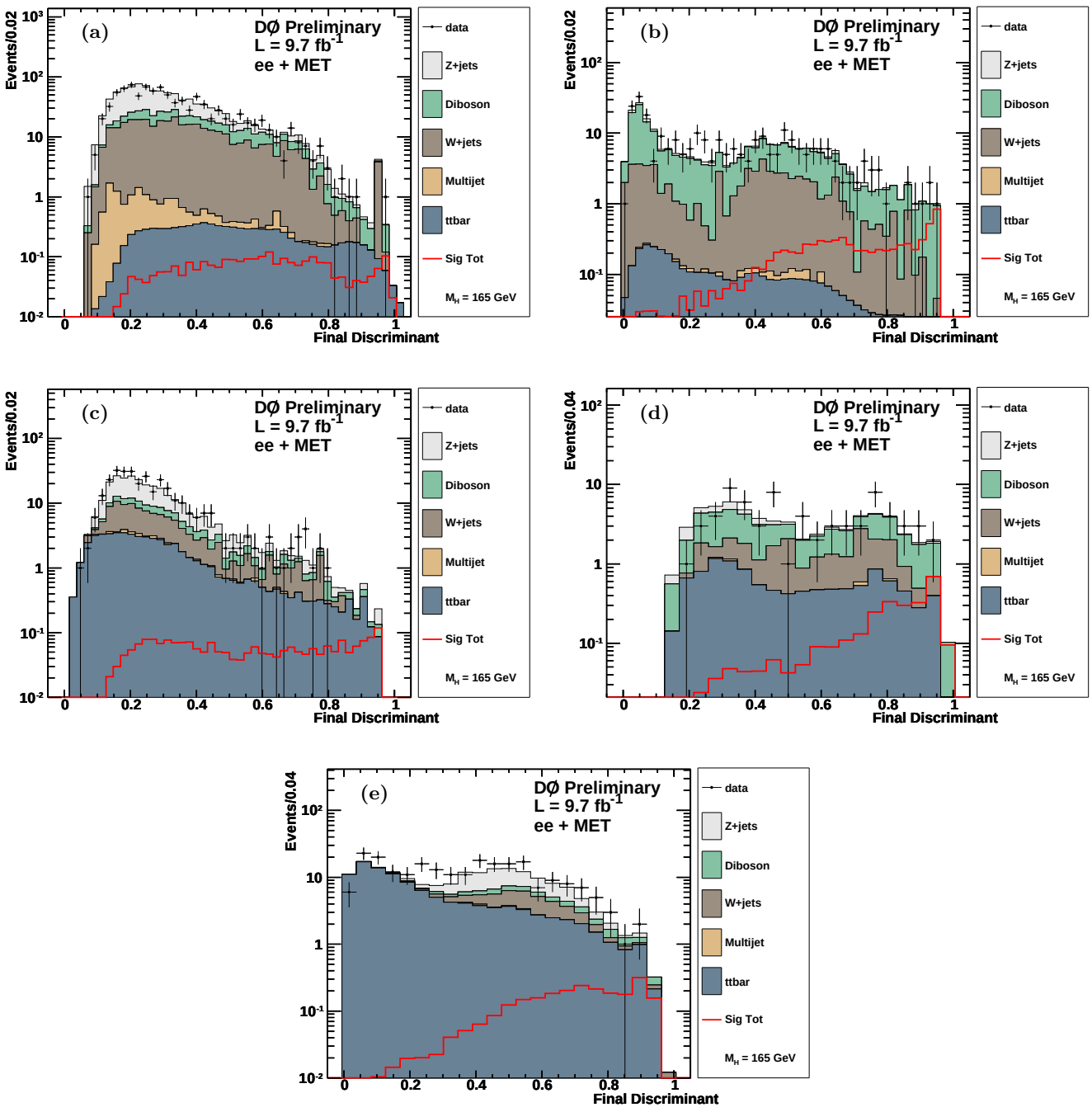

FIG. 15: The final BDT discriminant for $M_H = 165$ GeV for the e^+e^- channel with (a) no jet WW-depleted, (b) no jet WW-enriched, (c) one jet WW-depleted, (d) one jet WW-enriched and (e) equal or more than 2 jets.

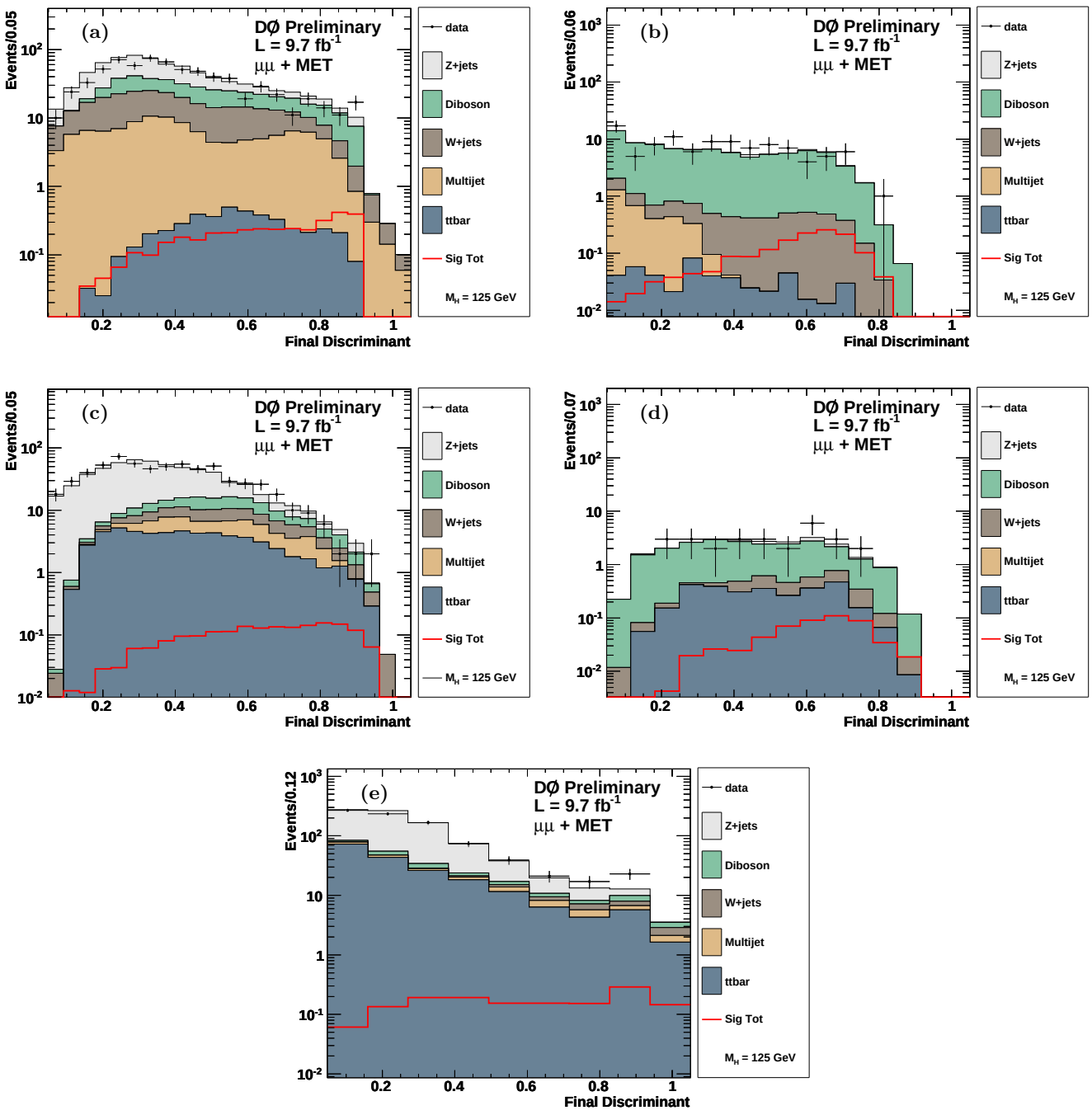

FIG. 16: The final BDT discriminant for $M_H = 125$ GeV for the $\mu^+\mu^-$ channel with (a) no jet WW-depleted, (b) no jet WW-enriched, (c) one jet WW-depleted, (d) one jet WW-enriched and (e) equal or more than 2 jets.

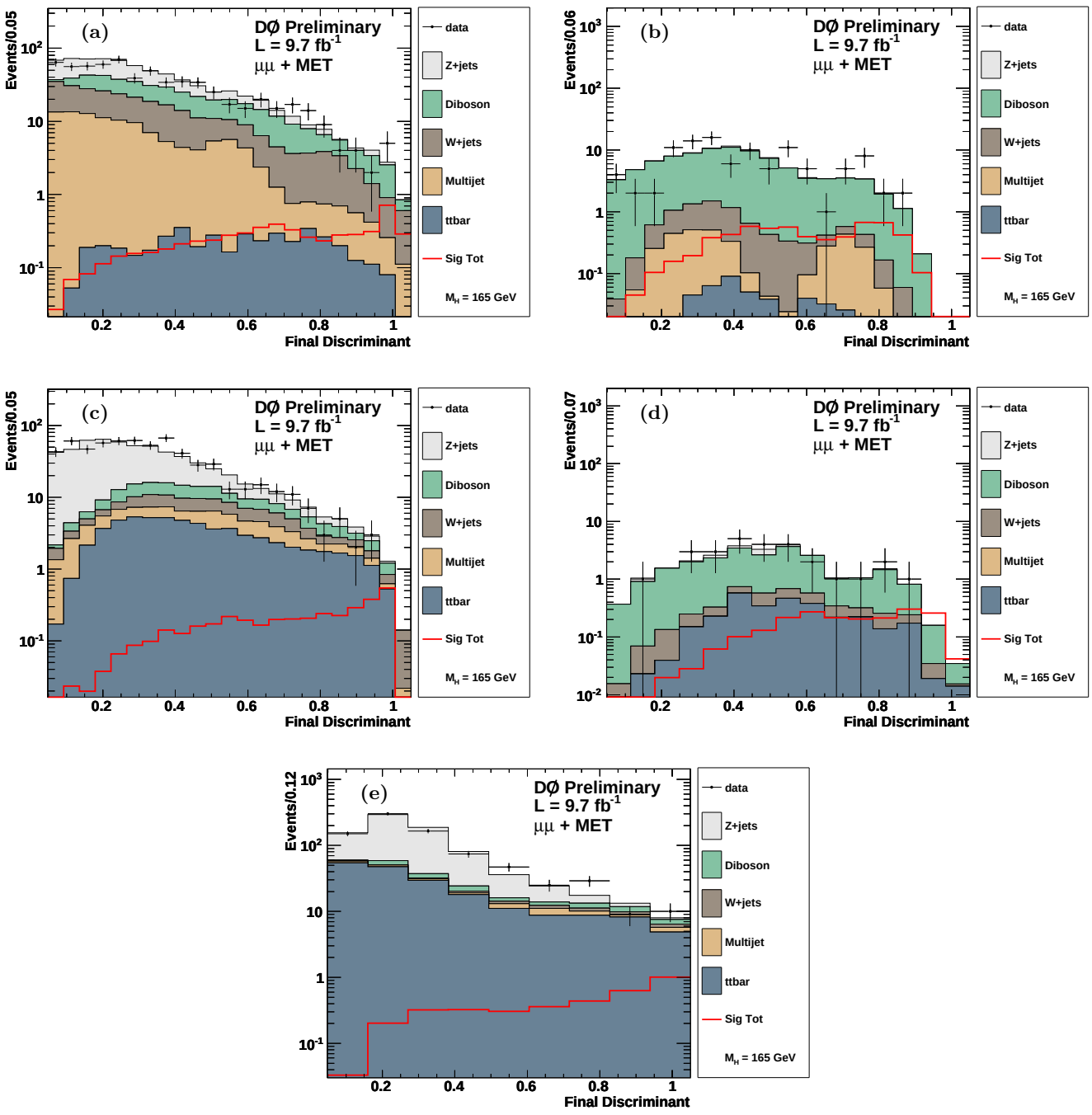

FIG. 17: The final BDT discriminant for $M_H = 165$ GeV for the $\mu^+\mu^-$ channel with (a) no jet WW-depleted, (b) no jet WW-enriched, (c) one jet WW-depleted, (d) one jet WW-enriched and (e) equal or more than 2 jets.

TABLE III: Expected and observed upper limits at 95% CL for $\sigma(p\overline{p} \to H + X)$ relative to the SM for the total combination and separately for the e^+e^-, $e^\pm\mu^\mp$ and $\mu^+\mu^-$ channels in Run II for M_H between 115 and 200 GeV.

M_H	115	120	125	130	135	140	145	150	155	160	165	170	175	180	185	190	195	200
Exp. all:	7.06	5.01	3.59	2.89	2.33	2.00	1.70	1.46	1.22	0.89	0.81	0.99	1.20	1.44	1.87	2.32	2.66	3.16
Obs. all:	10.98	6.52	4.56	3.22	3.27	2.74	1.88	1.70	1.48	1.01	0.98	1.17	1.73	1.63	2.03	2.63	3.29	4.46
Exp. $e^\pm\mu^\mp$:	11.55	7.26	5.22	4.15	3.35	2.86	2.38	2.11	1.73	1.27	1.19	1.47	1.74	2.10	2.64	3.25	3.93	4.65
Obs. $e^\pm\mu^\mp$:	12.94	7.28	4.87	4.45	3.93	2.65	2.09	1.82	1.60	1.16	1.33	1.51	1.87	2.00	2.87	3.33	3.89	4.55
Exp. e^+e^-:	12.43	9.75	6.89	5.36	4.28	3.96	3.15	2.72	2.32	1.75	1.59	1.91	2.20	2.72	3.36	4.03	4.82	5.47
Obs. e^+e^-:	11.70	10.34	9.16	4.79	5.55	5.37	4.01	3.69	2.73	2.04	1.64	1.97	2.82	3.12	3.44	5.22	6.47	8.33
Exp. $\mu^+\mu^-$	13.32	9.55	6.76	5.12	4.35	3.59	3.23	2.91	2.54	1.91	1.64	2.12	2.47	3.08	4.01	4.78	5.65	6.62
Obs. $\mu^+\mu^-$	26.72	16.37	9.92	7.70	6.97	6.29	5.24	5.10	4.72	3.10	2.53	3.53	4.49	4.93	5.40	6.31	8.30	10.46

VII. SYSTEMATIC UNCERTAINTIES

Sources of systematic uncertainties that affect only the normalization are: overall normalization uncertainty due to theoretical cross sections of Z+jets (4%); theoretical cross section for W+jets (6%), diboson (6%) and $t\bar{t}$ (7%); multijet normalization (30%); W+jets overall normalization ($15-30$%); a Z+jets jet bin dependent normalization ($2-15$%); and jet bin dependent modeling of the Z+jets background and the $\not\!\!E_T$ (5-19%). The signal $gg \to H$ cross-section has different scale and PDF uncertainties depending on the reconstructed jet bin. Using the prescription described in Ref. [37], the $gg \to H$ cross-section scale/PDF uncertainties range between 13-33%/7.6-30%, depending on the jet bin. We also consider sources of systematic uncertainty which affect the shape of the final discriminant distribution (and quote here the average fractional change across bins of the final discriminant distribution for all backgrounds): jet energy scale (4%); jet resolution (0.5%); jet identification (2%); jet association to primary vertex (vertex confirmation) (2%) and b-tagging for the heavy-flavor $t\bar{t}$ sample (4%). Several systematic uncertainties are included which have a small (< 1%) effect on the background model: modeling of diboson production in terms of $p_{\rm T}(WW)$ and $\Delta\phi$ between the leptons, and the $p_{\rm T}$ of the vector boson from W+jets and Z+jets production. The shape change in the BDT distribution for background due to PDF uncertainties was found to be small and flat. It is taken into account as a 2% systematic uncertainty for all background MC samples. In the e^+e^- and $\mu^+\mu^-$ channels, we assign a 2-4% systematic uncertainty to the splitting of the 0 jet and 1 jet multiplicity bins into WW-depleted and WW-enriched regions for WW and $gg \to H \to WW$.

VIII. LIMITS

The BDT output distributions in data agree within uncertainties with the expected backgrounds as shown in Fig. 12-17. The BDT output distributions are therefore used to set limits on the Higgs boson inclusive production cross section $\sigma(p\overline{p} \to H + X)$ assuming SM values for the branching ratios and for the relative cross sections of the various Higgs production mechanisms considered [38]. We calculate limits using a modified frequentist method (CLs), with a log-likelihood ratio (LLR) test statistic [39]. To achieve maximal sensitivity in the combined limit, the thirteen individual inputs (three leptonic channels, three jet bins for $e^\pm\mu^\mp$ and five sub-channels for e^+e^- and $\mu^+\mu^-$) are treated separately. To minimize the degrading effects of systematics on the search sensitivity, the individual background contributions are fit to the data observation by maximizing a profile likelihood function for the background-only and signal-plus-background hypotheses [40].

Table III presents expected and observed upper limits at 95% CL for $\sigma(p\overline{p} \to H + X)$ relative to that expected in the SM for each Higgs boson mass considered. Fig. 18 shows expected and observed limits for $\sigma(p\overline{p} \to H + X)$ relative to the SM for different Higgs boson masses, while Fig. 19 shows the corresponding LLR distributions. For $M_H = 165$ GeV (125 GeV), the expected limit is 0.81 (3.59) relative to the Standard Model yield and the observed limit reaches 0.98 (4.56) in the same units.

IX. CONCLUSIONS

A search for the standard model Higgs boson in dilepton ($e^\pm\mu^\mp$, e^+e^-,$\mu^+\mu^-$) events with large missing transverse energy using 9.7 fb^{-1} of $p\overline{p}$ collisions at $\sqrt{s} = 1.96$ TeV, collected with the DØ detector at the Fermilab Tevatron collider was presented. No significant excess above standard model background expectations was observed, and upper limits on Higgs boson production were derived. We also exclude a Higgs boson with a mass $M_H = 165$ GeV.

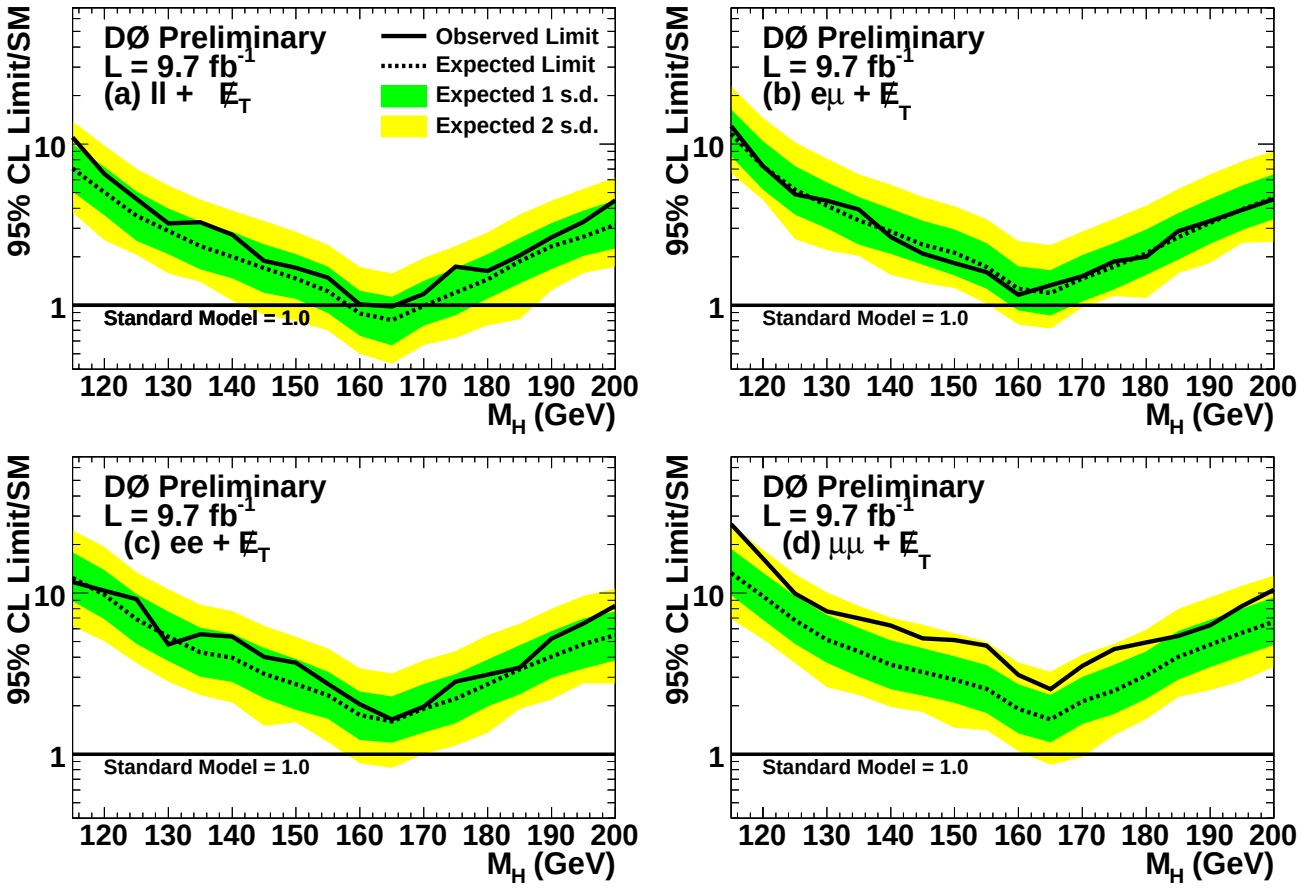

FIG. 18: Excluded cross section ($\sigma(p\overline{p} \to H + X)$) at 95% CL in units of the SM cross section as a function of M_H using (a) all channels, (b) $e^{\pm}\mu^{\mp}$ channel, (c) $e^{+}e^{-}$ channel, (d) $\mu^{+}\mu^{-}$ channel.

[1] R. Barate *et al.*, Phys. Lett. **B 565**, 61 (2003).
[2] The TEVNPH Working Group, arXiv:1203.3774 [hep-ex].
[3] ATLAS Collaboration, G. Aad *et al.*, arXiv:1202.1408 [hep-ex], Phys. Lett. **B 710** (2012) 49-66.
[4] CMS Collaboration, S. Chatrchyan *et al.*, Phys. Lett. **B 710**, 91 (2011).
[5] CDF Collaboration, T. Aaltonen *et al.*, Phys. Rev. Lett. **108**, 151803 (2012).
[6] DØ Collaboration, V. Abazov *et al.*, Phys. Rev. Lett. **108**, 151804 (2012).
[7] The LEP Electroweak Working Group, "Status of March 2012", http://lepewwg.web.cern.ch/LEPEWWG/
[8] DØ Collaboration, V. Abazov *et al.*, Phys. Rev. Lett. **104**, 061804 (2010).
[9] DØ Collaboration, V. Abazov *et al.*, DØ conference note 6302.
[10] DØ Collaboration, V. Abazov *et al.*, Nucl. Instrum. Methods Phys. Res. **A 565**, 463 (2006).
[11] S.N. Ahmed *et al.*, Nucl. Instrum. Methods Phys. Res. **A 634**, 8 (2011).
[12] R. Angstadt *et al.*, Nucl. Instrum. Methods Phys. Res. **A 622**, 298 (2010).
[13] M. Abolins *et al.*, Nucl. Instrum. Methods Phys. Res. A **584**, 75 (2008).
[14] T. Andeen *et al.*, Report. No. FERMILAB–TM–2365 (2007).
[15] T. Sjöstrand *et al.*, Comp. Phys. Comm. **135**, 238 (2001), we use version 6.323 or later.
[16] M.L. Mangano, M. Moretti, F. Piccinini, R. Pittau, A. Polosa, J. High Energy Phys. **0307**, 001 (2003), we use version 2.11.
[17] J. Pumplin et al., J. High Energy Phys. **07**, 012 (2002).
[18] R. Brun and F. Carminati, CERN Program Library Long Writeup W5013, 1993 (unpublished).
[19] D. Florian and M. Grazzini, Phys. Lett. **B 674** 291-294 (2009).
[20] J. Baglio and A. Djouadi, J. High Energy Phys. **10**, 064 (2010).
[21] P. Bolzoni *et al.*, Phys. Rev. Lett. **105**, 011801 (2011).

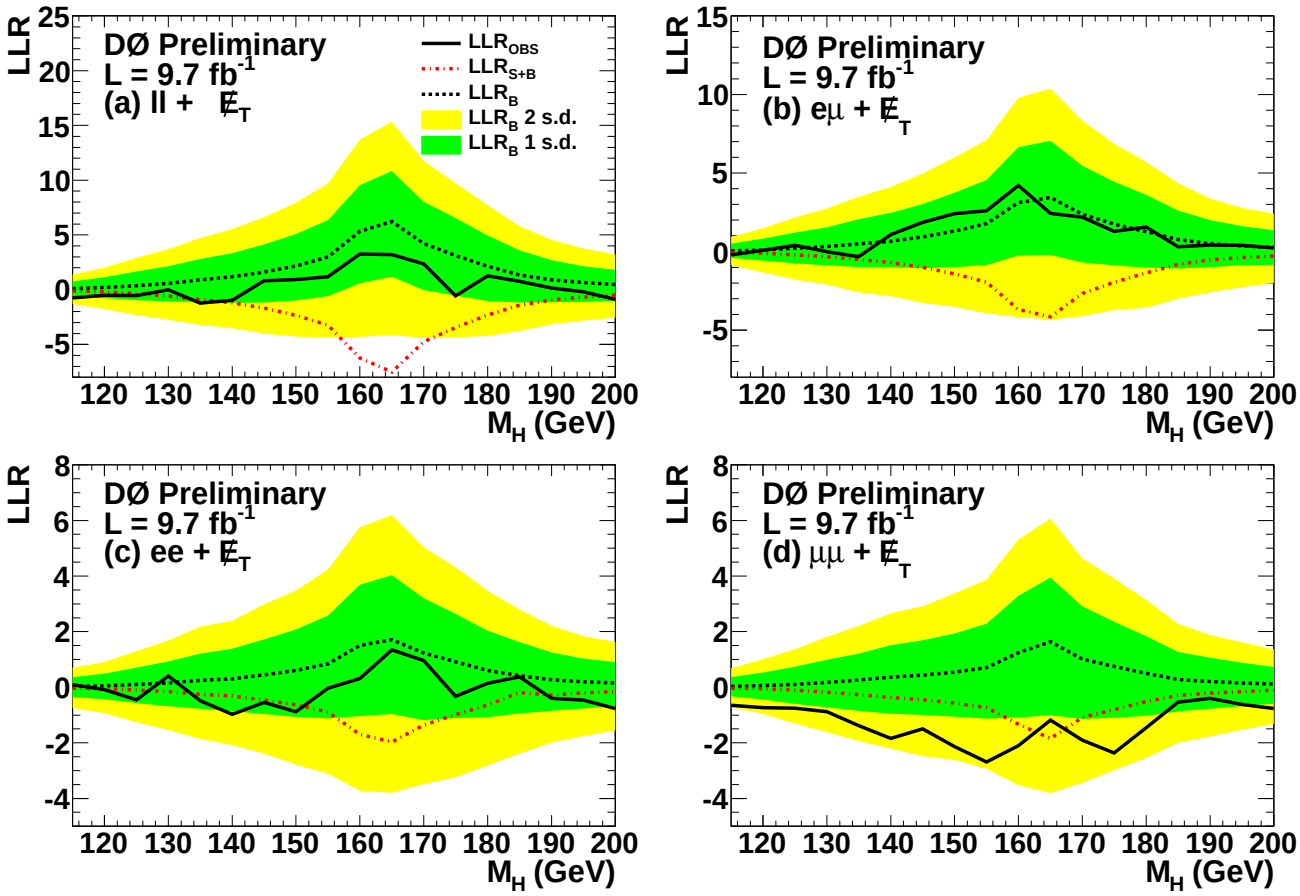

FIG. 19: The observed LLR (solid line) as a function of M_H using (a) all channels, (b) $e^{\pm}\mu^{\mp}$ channel, (c) e^+e^- channel, (d) $\mu^+\mu^-$ channel. Also shown are the expected LLRs for the Background (black dashed line) and Signal+Background (red dashed line) hypotheses, with the green and yellow bands indicating one and two sigma fluctuations of the expected LLR for the Background-only hypothesis.

[22] A. D. Martin, W. J. Stirling, R. S. Thorne and G. Watt, Eur. Phys. J. **C 63**, 189 (2009) [arXiv:0901.0002 [hep-ph]]
[23] S. Alekhin *et al.*, arXiv:1101.0536v1 [hep-ph]; M. Botje *et al.*, arXiv:1101.0538v1 [hep-ph].
[24] G. Bozzi, S. Catani, D. de Florian, M. Grazzini, Phys. Lett. **B 564** (2003) 65 [hep-ph/0302104]; Nucl. Phys. **B 737** (2006) 73 [hep-ph/0508068].
[25] R. Hamberg, W.L. van Neerven, and T. Matsuura, Nucl. Phys. **B 359**, 343 (1991) [Erratum-ibid. **B644**, 403 (2002)].
[26] DØ Collaboration, V. Abazov *et al.*, Phys. Rev. Lett. 100, 102002 (2008).
[27] K. Melnikov and F. Petriello, Phys. Rev. **D 74**, 114017 (2006).
[28] U. Langenfeld, S. Moch and P. Uwer, Phys. Rev. **D 80**, 054009 (2009) [arXiv:0906.5273 [hep-ph]], we use $\sigma(t\bar{t}) = 7.04$ pb (calculated using $m_t = 173 \pm 1.2$ GeV and the MSTW2008 PDF set).
[29] J. Campbell and R. K. Ellis, Phys. Rev. **D 60**, 113006 (1999). We use MCFM tool (http://mcfm.fnal.gov/) with $\sigma(WW) =$ 11.34 pb, $\sigma(WZ) = 3.45$ pb and $\sigma(ZZ) = 1.5$ pb.
[30] S. Frixione and B.R. Webber, J. High Energy Phys. **0206**, 029 (2002) [hep-ph/0204244].
[31] T. Binoth, M. Ciccoli, N. Kauer, M. Krämer, J. High Energy Phys. **0503**, 065 (2005), J. High Energy Phys. **0612**, 046 (2006).
[32] G.C. Blazey *et al.*, [hep-ex/0005012] (2000).
[33] DØ Collaboration, V. Abazov *et al.*, Phys. Rev. Lett. **101**, 062001 (2008).
[34] A. Hoecker, P. Speckmayer, J. Stelzer, J. Therhaag, E. von Toerne, and H. Voss, "TMVA 4 Toolkit for Multivariate Data Analysis with ROOT Users Guide" [physics/0703039a].
[35] C.G. Lester, D.J. Summers, Phys. Let. **B 463**, 99-103, (1999); H. Cheng, Z. Han, J. High Energy Phys. **12**, 063 (2008).
[36] DØ Collaboration, V. Abazov *et al.*, Nucl. Instrum. Methods Phys. Res. **A 620**, 490 (2010).
[37] DØ Collaboration, V. Abazov *et al.*, DØ Conference Note 6229 (2011).
[38] S. Dittmaier *et al.* [LHC Higgs Cross Section Working Group], Handbook of LHC Higgs Cross Sections: 1. Inclusive Observables, arXiv:1101.0593v2 [hep-ph].

[39] T. Junk, Nucl. Instrum. Methods Phys. Res. **A 434** 435 (1999). A. Read, CERN 2000-005 (30 May 2000).
[40] W. Fisher, FERMILAB-TM-2386-E (2006).